

Check for updates

## **Dynamic Regulation of Adaptive Butterfly-Shaped Molecules** via B←N Coordination

Boyu Wang, Yani Huo, Cheng Chen, Xiao-Ye Wang, \* Chuancheng Jia, \* Jinying Wang, \* and Xuefeng Guo\*

Achieving dynamic control over stereostructures and electronic properties of rigid molecules remains a significant challenge due to the delicate balance between stability and flexibility. Here, the construction of butterfly-shaped molecular junctions stabilized by moderate-strength boron-nitrogen (B←N) coordination between boraacenes and pyridines is reported. By leveraging the pivot-like flexibility of B←N bonds, molecular conductance switching with on/off ratios exceeding 100 is achieved through force-driven dynamic transitions between distinct stacking conformations. Single-molecule electrical measurements combined with first-principle calculations identify distinct charge transport mechanisms—through-space and through-bond—associated with the butterfly-wing open and closed configurations. Furthermore, external factors like electric fields and substituent effects modulate  $\pi$ - $\pi$  interactions and charge transport properties. The introduction of destructive quantum interference effects can be achieved by replacing molecular units. The findings demonstrate that B←N coordination serves as a dynamically tunable linkage, offering a pathway to design molecular platforms with multifunctional units, customized stereo-conformations, and quantum effects.

1. Introduction

Precise dynamic regulation of molecular stereostructures is essential for achieving intelligent molecular responses, which expands their applications in molecular electronics, optoelectronics, and smart materials.[1-3] Noncovalent interactions facilitate the construction of multiunit molecules with tunable stereo-conformations, enabling dynamic modulation of electronic properties in response to external stimuli.[4,5] For example, supramolecular ratchets exhibit dynamic conformational switching of foldamers under mechanical control,[6] offering practical applications in biomimetic molecular machines and energy transduction systems.[7,8] These supramolecular interactions allow for sophisticated tuning of spatial electronic coupling through stacking sites,[9] as well as orbital overlaps,[10,11] paving the way for integrable molecular circuits and quantum manipulation.[12,13] However, achieving dynamic regulation of small multiunit molecules remains a significant challenge, particularly for those with rigid and intricate structures.[14-16] The intrinsic tension of these molecules hinders stable dynamic regulation, limiting the development of functionally responsive and dynamically adaptable systems. [17,18]

Classic Lewis acid-base boron-nitrogen (B←N) interactions offer a promising alternative for the dynamic regulation of molecular architectures due to their adaptive

nature and unique properties. These medium-strength dative bonds balance the stability and flexibility, allowing seamless integration of multifunctional units without compromising the structural integrity.[19] Moreover, their rotational adjustability ensures stable dynamic responses to external stimuli, offering precise and durable tuning of spatial electronic characteristics. [20,21] Despite great progress in utilizing B←N interactions in organic semiconductors and photonic devices, [22,23] the potential for

B. Wang, Y. Huo, C. Jia, J. Wang, X. Guo Center of Single-Molecule Sciences Institute of Modern Optics Frontiers Science Center for New Organic Matter Tianjin Key Laboratory of Micro-Scale Optical Information Science and Technology College of Electronic Information and Optical Engineering Nankai University 38 Tongyan Road, Jinnan District, Tianjin 300350, P. R. China E-mail: jiacc@nankai.edu.cn; wangjynk@nankai.edu.cn; guoxf@pku.edu.cn

The ORCID identification number(s) for the author(s) of this article can be found under https://doi.org/10.1002/adma.202504455

Academy for Advanced Interdisciplinary Studies Haihe Laboratory of Sustainable Chemical Transformations College of Chemistry Nankai University 94 Weijin Road, Nankai District, Tianjin 300071, P. R. China E-mail: xiaoye.wang@nankai.edu.cn Beijing National Laboratory for Molecular Sciences National Biomedical Imaging Center College of Chemistry and Molecular Engineering Peking University 292 Chengfu Road, Haidian District, Beijing 100871, P. R. China

State Key Laboratory of Elemento-Organic Chemistry

Frontiers Science Center for New Organic Matter

DOI: 10.1002/adma.202504455

C. Chen, X.-Y. Wang

15214095, 0, Downloaded from https://advanc

onlinelbary. wiley.com/doi/10.1002/atma.202504355 y Peking University Health, Wiley Online Library on [02/11/2025]. See the Terms and Conditions (https://onlinelbbrary.wiley.com/terms-and-conditions) on Wiley Online Library for rules of use; OA articles are governed by the applicable Creative Commons License

Figure 1. Design and switching of butterfly-shaped boron-nitrogen ( $B \leftarrow N$ ) dative structures. a) Schematic representation of  $B \leftarrow N$  coordination between boraacene and borapentacene functionalized with dimethylthiophenyl groups and double pyridines. The R group denotes various substituents. b) Schematic representation of mechanical force-driven switching of butterfly-shaped structures. The  $B \leftarrow N$  coordinated structures undergo transitioning between two stable states with distinct  $\pi - \pi$  stacking configurations, analogous to a butterfly's wings in open and closed positions, during stretching and compression cycles.

dynamic structural and electronic regulation in small molecules remains underexplored. Single-molecule junctions serve as a powerful technique for probing the adaptive nature of  $B \leftarrow N$  molecules, facilitating multimodal regulation and high-precision monitoring of charge transport, thus advancing the development of multifunctional responsive systems. [24,25]

In this study, boron-embedded polycyclic aromatic hydrocarbons and 4-substituted pyridine derivatives are employed as electron-acceptor and electron-donor units, respectively, to construct butterfly-shaped multifunctional molecular systems via  $B \leftarrow N$  coordination (Figure 1a). Scanning tunneling microscopybreak junction (STM-BJ) techniques provide precise mechanical control over the open and closed conformations of the butterfly-shaped structures. In combination with first-principle calculations, the  $B \leftarrow N$  interactions and charge transport mechanisms are elucidated at the single-molecule level. This approach, utilizing dynamic regulation of multiunit stereo-conformations via dative  $B \leftarrow N$  bonds, significantly broadens molecular design possibilities and establishes a versatile platform for realizing advanced molecular functionalities and enhanced performance.

### 2. Results and Discussion

### 2.1. Design of Butterfly-Shaped B←N Structures

Multiunit molecules with dative B←N bonds are prepared by the addition of boraacene and borapentacene-based precursors with multiple 4-substituted pyridines.<sup>[27]</sup> Notably, an all-carbon acene molecule is employed as a control to comparatively highlight the necessity of boron sites in forming butterfly-shaped structures with tunable stacking conformations.<sup>[28]</sup> The synthesis and structural characterization of all precursors and control molecules are provided in Schemes S1 and S2, and Figures S1-S8 (Supporting Information), including <sup>1</sup>H, <sup>13</sup>C, and <sup>11</sup>B NMR spectra. Notably, the <sup>11</sup>B NMR spectra provide clear evidence for the successful formation of sp<sup>3</sup>-hybridized boron centers in the B←N adducted structures (Figures \$9 and \$10, Supporting Information). Mass spectrometry is utilized to verify the formation of doubly incorporated B←N coordinated structures (Figure S11, Supporting Information). Additionally, UV-vis absorption spectroscopy titration (Figure S12, Supporting Information) and pyridine concentration-dependent STM-BJ experiments (Figures

15214095, 0, Downloaded from https://advanced

onlinelibrary.wiley.com/doi/10.1002/adma.202504455 by Peking University Health, Wiley Online Library on [02/11/2025]. See the Terms and Conditions (https://onlinelibrary.wiley.com/erns

and-conditions) on Wiley Online Library for rules of use; OA articles are governed by the applicable Creative Commons License

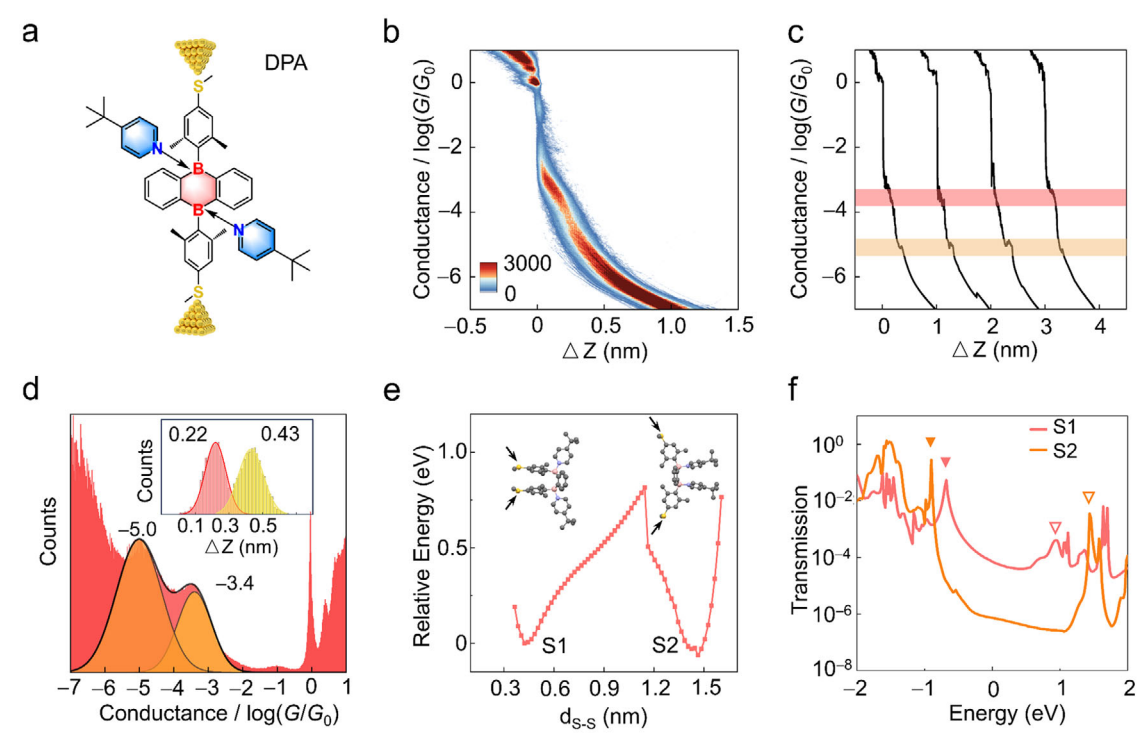


Figure 2. Single-molecule electrical measurements and theoretical analyses of DPA junctions. a) Schematic diagram of the DPA junction with gold electrodes. b) 2D conductance-displacement histograms of DPA obtained from STM-BJ measurements. The color bar represents the number of counts. c) Representative single-molecule conductance traces of DPA, exhibiting two distinct conductance states. d) 1D conductance histograms of DPA junctions, highlighting the bistable molecular states. The inset shows the normalized plateau-length distributions, measured in respective ranges. e) Relaxed coordinate scan of the potential energy surface for DPA with varying sulfur-sulfur distances. The inset shows the schematic diagram of S1-DPA and S2-DPA under exerted forces. f) Theoretical transmission spectra of S1-DPA and S2-DPA junctions, with triangles marking the transmission peaks corresponding to p-HOMOs and p-LUMOs.

# S13–S16, Supporting Information) are conducted to monitor the addition dynamics of $B \leftarrow N$ molecules.

Using the dative  $B \leftarrow N$  bonds as flexible joints, a doubly  $B \leftarrow N$ embedded molecular structure with paired thiomethylphenylgold contacts is further designed, which is expected to exhibit two distinct stacking configurations under mechanical forces (Figure 1b; Tables S1 and S2, Supporting Information). Unlike covalent B-N bonds that are relatively rigid and weakly polarized, the dative B←N coordination features the moderate bond strength with adaptability and pronounced polarity, alleviating the intramolecular strain while providing the flexibility required for reversible conformational switching (Figure S17, Supporting Information). Specifically,  $\pi$ – $\pi$  interactions between the thiomethylphenyl rings induce the expansion of the pyridine rings, mimicking a butterfly opening its wings. Upon stretching the molecular backbone, the configuration transitions to the other state where the pyridine rings stably stack, analogous to a butterfly closing its wings (Figure S18, Supporting Information).<sup>[29]</sup> The B←N coordinated structure provides a unique platform for exploring multiunit molecules with intricate stereostructures and examining the impact of noncovalent interactions on the stacking and electronic characteristics of  $\pi$  systems (Figure S19 and Table S3, Supporting Information).[30]

# 2.2. Exploring Charge Transport Characteristics of $B \leftarrow N$ Coordinated DPA Junctions

Given the adaptive nature of butterfly-shaped B←N molecular structures, dynamic changes in molecular electronic characteristics are anticipated and examined using the STM-BJ technique.[31] Single-molecule conductance (G) is measured in а 1,2,4-trichlorobenzene (TCB) solution containing 0.1 mм of target molecules, with the dynamic single-molecule junctions formed by manipulating the tip. During repeated junction formations, conductance plateaus are found in individual traces, with G values exhibiting a negative exponent of  $G_0$  (where  $G_0 = 2e^2 h^{-1}$ ). Figure 2a illustrates the chemical structure of the double 4-tertbutylpyridine (t-BuPy) adduct of 1,4-dihydrodiboraanthracene (DPA). Pyridines with larger steric hindrance are employed to prevent the formation of dissociated pyridine dimers (Figure S20, Supporting Information). Figure 2b presents the 2D conductance histograms constructed from ≈9000 single traces of DPA. In contrast to the exponential decay characteristics observed in the 2D conductance-displacement histograms of pure TCB and t-BuPy control experiments (Figures S21-S23, Supporting Information), the 2D histograms of the molecular solutions display distinct single-molecule conductance plateaus. Representative individual traces at 0.1 V reveal two isolated conductance

15214095, 0, Downloaded from https://advan

onlinelibrary.wiley.com/doi/10.1002/adma.202504455 by Peking University Health, Wiley Online Library on [02/11/2025]. See the Terms and Conditions (https://onlinelibrary.wiley.com/erms

-conditions) on Wiley Online Library for rules of use; OA articles are governed by the applicable Creative Commons License

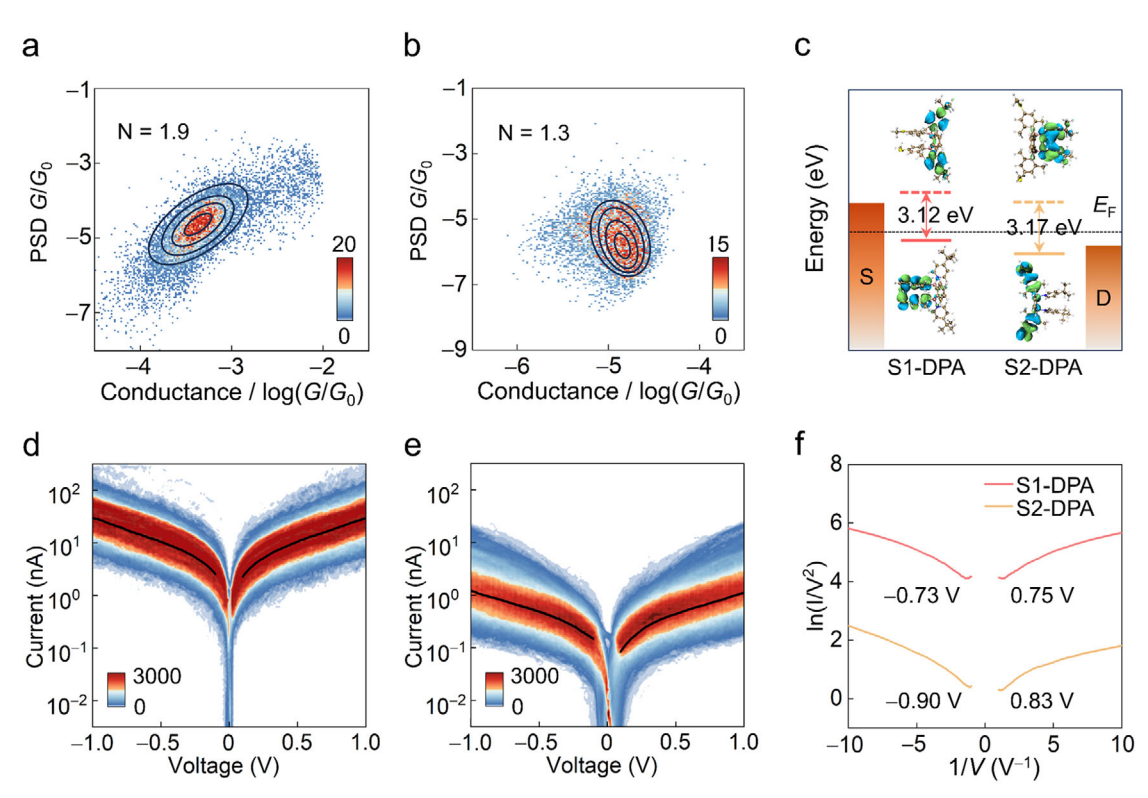


Figure 3. Charge transport characteristics of the bistable states of DPA. a, b) 2D histograms of normalized noise power versus average conductance for S1-DPA (a) and S2-DPA (b), respectively. c) Molecular frontier orbitals of S1-DPA and S2-DPA (HOMO: lower insets; LUMO: upper insets) and their energies with respect to the Fermi level of gold electrodes. d, e) 2D current-voltage (*I*–*V*) histograms for S1-DPA (d) and S2-DPA (e), respectively. f) Fowler–Nordheim plots derived from the fitted *I*–*V* curves (black lines in Figure 3d,e). The transition voltages for both positive and negative polarities are marked.

plateaus (Figure 2c). These plateaus can be identified through Gaussian fitting in the 1D conductance histograms (Figure 2d). Specifically, a shorter high-conductance state at  $\approx$ 4.0 × 10<sup>-4</sup>  $G_0$  ( $\approx$ 31.0 nS) with a length of 0.22 nm (S1-DPA) and a longer low-conductance state at  $\approx$ 1.0 × 10<sup>-5</sup>  $G_0$  ( $\approx$ 0.77 nS) with a plateau length of 0.43 nm (S2-DPA) are observed. [15]

To clarify the origin of the distinct molecular conductance states, a relaxed potential energy surface scan between the sulfur atoms in the thiomethyl groups is performed to simulate the forces applied between the Au-S contacts of junctions. Two stable states, designated as S1 and S2 stacking modes of DPA, are identified, displaying the butterfly-shaped closed and open B←N structures (Figure 2e). A side-by-side comparison between the B←N coordinated structures and the control analogues further highlights the indispensable role of B←N bonds in enabling such conformational transitions (Figure S24, Supporting Information). In addition to the stacking stabilization, the variation in B←N bond length also correlates with the energy profile of the switching process, underscoring its flexible yet crucial role in enabling conformational transitions (Figure S25, Supporting Information). Notably, both plateau lengths of S1-DPA and S2-DPA are shorter than the theoretical S-S distances, which may be attributed to the combined effects of electrode snap-back and the dynamic nature of butterfly-shaped molecular junctions.<sup>[32]</sup> The transmission spectra of S1-DPA and S2-DPA molecular junctions align well with the experimental electrical measurements

(Figure 2f; Figures S26 and S27, Supporting Information). Energy barrier analysis supports the feasibility of force-induced state transitions between stereo-conformations, driven by the mechanical force applied by the STM-BJ gold electrodes (Figure S28, Supporting Information). The perturbed highest occupied molecular orbitals (p-HOMOs) of both S1-DPA and S2-DPA junctions are found to be the dominant transport channels, as they are positioned closer to the Fermi level of the gold electrodes. [32,33] Theoretical transmission analyses of the precursors and other byproducts show no bistable conductance states, further supporting that the distinct conductance states arise from dynamic transitions between butterfly-shaped closed and open B←N structures (Figures S29 and S30, Supporting Information).

# 2.3. Through-Space Versus Through-Bond Charge Transport Mechanisms

To investigate the transport mechanisms of S1-DPA and S2-DPA, their transport pathways are examined using flicker noise analysis in combination with theoretical simulations. The hovering ranges for S1-DPA and S2-DPA are set identically at  $G^{1.6}$  ( $G^{-2.6 \text{ to} -4.2}$  for S1-DPA, and  $G^{-4.2 \text{ to} -5.8}$  for S2-DPA). **Figure 3a** shows the power spectral density (PSD) for S1-DPA at N=1.9, while Figure 3b shows that of S2-DPA at N=1.3 (Figure S31, Supporting Information). These distinct PSD results indicate

15214095, 0, Downloaded from https://advanc

onlinelibrary.wiley.com/doi/10.1002/adma.202504455 by Peking University Health, Wiley Online Library on [02/11/2025]. See the Terms and Conditions (https://onlinelibrary.wiley.com/doi/10.1002/adma.202504455 by Peking University Health, Wiley Online Library on [02/11/2025]. See the Terms and Conditions (https://onlinelibrary.wiley.com/doi/10.1002/adma.202504455 by Peking University Health, Wiley Online Library on [02/11/2025]. See the Terms and Conditions (https://onlinelibrary.wiley.com/doi/10.1002/adma.202504455 by Peking University Health, Wiley Online Library on [02/11/2025]. See the Terms and Conditions (https://onlinelibrary.wiley.com/doi/10.1002/adma.202504455 by Peking University Health, Wiley Online Library on [02/11/2025]. See the Terms and Conditions (https://onlinelibrary.wiley.com/doi/10.1002/adma.202504455 by Peking University Health, Wiley Online Library on [02/11/2025]. See the Terms and Conditions (https://onlinelibrary.wiley.com/doi/10.1002/adma.202504455 by Peking University Health, Wiley Online Library on [02/11/2025]. See the Terms and Conditions (https://onlinelibrary.wiley.com/doi/10.1002/adma.202504455 by Peking University Health, Wiley Online Library on [02/11/2025]. See the Terms and Conditions (https://onlinelibrary.wiley.com/doi/10.1002/adma.202504455 by Peking University Health, Wiley Online Library on [02/11/2025].

conditions) on Wiley Online Library for rules of use; OA articles are governed by the applicable Creative Commons

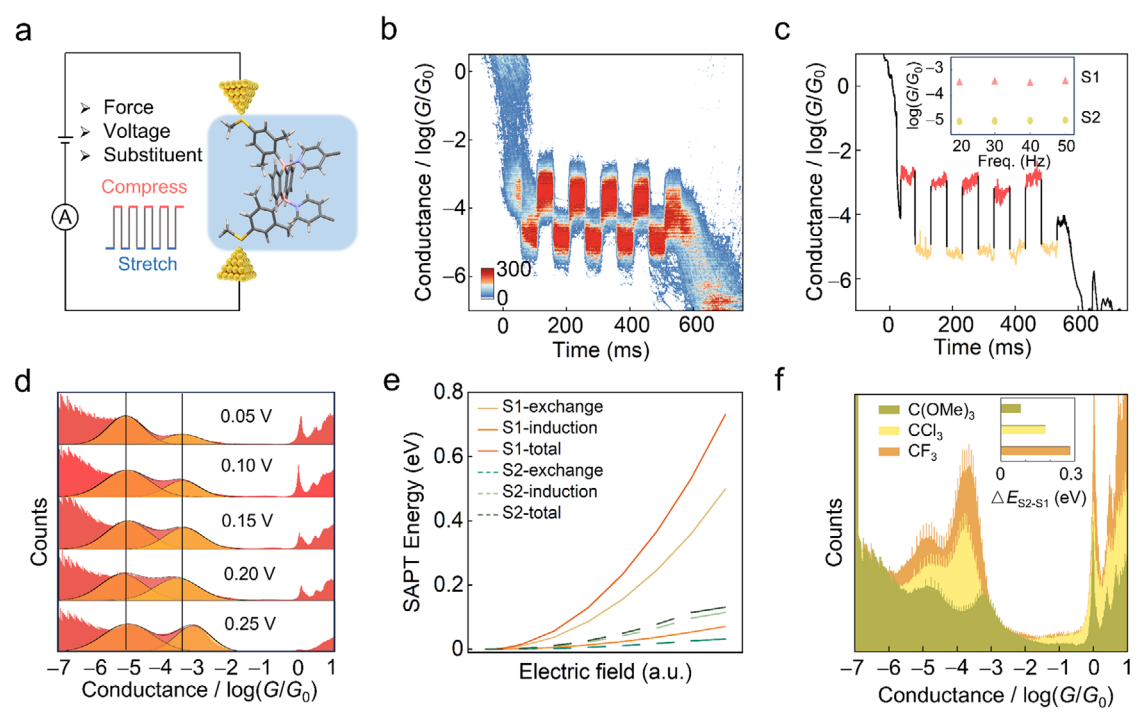


Figure 4. Multimodal regulation of charge transport in B←N molecular junctions. a) Schematic diagram of B←N junctions under piezo voltage-controlled square-wave oscillations and other regulation strategies. b) 2D conductance-time histograms of DPA under square-wave oscillations at 20 Hz. c) Representative single conductance-time trace of DPA under square-wave oscillations, with S1 and S2 states highlighted in different colors. Inset: Oscillation frequency ranges from 20 to 50 Hz, showing nearly identical switching behavior. d) 1D conductance histograms of DPA under electric fields ranging from 0.05 to 0.25 V in 0.05 V increments. e) Energy components of S1 and S2 DPA, including exchange energy, induction energy, and total interaction energy, calculated for different stereo-conformations under an external electric field using the symmetry-adapted perturbation theory. f) 1D conductance histograms of various B←N structures with different pyridine substituents. Inset: relative binding energy differences between S1 and S2 DPA of pyridine with various substituents.

that the open butterfly-wing conformation of the S1-DPA junction is primarily governed by through-space transport, whereas the closed butterfly-wing conformation of the S2-DPA junction is dominated by through-bond transport.[34-36] Frontier orbital calculations reveal that the different  $\pi$ - $\pi$  stacking stereoconformations lead to the HOMOs of S1-DPA and S2-DPA being primarily localized within the  $\pi$ - $\pi$  stacked thiomethylphenyl ring and the unfolded molecular backbone, respectively (Figure 3c). This demonstrates that the transport pathways are regulated by force-driven conformational changes, which are consistent with the transmission eigenstates and transmission pathway analysis (Figures S32 and S33, Supporting Information). Further theoretical analysis of the transition state reveals that the gradual unfolding of the molecular backbone drives the switch from throughbond to through-space charge transport (Figure \$34, Supporting Information).

To explore the electronic characteristics of the different  $B \leftarrow N$  stereo-conformations, current–voltage (I-V) measurements are conducted. Figure 3d,e shows the 2D I-V histograms of S1-DPA and S2-DPA junctions, respectively. From the I-V and extended conductance–voltage (G-V) measurements (Figure S35, Supporting Information), it is observed that the conductance of both S1-DPA and S2-DPA exhibits values similar to those shown in previous analyses. As the bias voltage increases, the conductance of both junctions rises, with S1-DPA displaying a higher rate of increase. This may result from the recovery of  $\pi-\pi$  stacking sym-

metry in *p*-HOMO of S1-DPA under an external electric field, as evident in the molecular projected self-consistent Hamiltonians (MPSHs) of the S1-DPA junction (Figures S36 and S37, Supporting Information). [37,38] The Fowler–Nordheim plots derived from the I-V measurements indicate a transition voltage of  $\approx 0.74$  V for S1-DPA and  $\approx 0.86$  V for S2-DPA (Figure 3f). [11,39] The orbital energy of S1-DPA being more closely aligned with the Fermi level than that of S2-DPA is consistent with the transmission spectra (Figure 2e) and orbital energy profiles (Figure 3c). These results reveal the intriguing, distinctive transport characteristics of B $\leftarrow$ N structures.

#### 2.4. Multimodal Dynamic Regulation of B←N Structures

The butterfly-shaped  $B \leftarrow N$  structures based on noncovalent stacking interactions provide a unique platform to investigate their response to external stimuli such as mechanical forces, electric fields, and substituent effects, thereby enabling dynamic multimodal tuning. **Figure 4a** illustrates the versatile strategies for dynamic control over the conductance states of the butterfly-shaped  $B \leftarrow N$  stereostructures. Direct switching between butterfly-wing open and closed conformations can be achieved by applying mechanical forces on the anchoring atoms. By applying square-wave mechanical oscillations via a piezocontrolled STM tip, the 2D conductance-time (G-t) histograms in

1521495, D. Dowloaded from https://advanced.onlinelibrary.wiley.com/oi/10.1002/adma.20204455 by Pebag University Health, Wiley Online Library on [02/11/2025] See the Terms and Conditions (https://onlinelibrary.wiley.com/errns-and-conditions) on Wiley Online Library for rules of use; OA articles are governed by the applicable Creative Commons License

Figure 4b display continuous conductance switching, with variations corresponding to the S1 and S2 states of DPA. The representative single trace exhibits conductance switching between  $\approx 1.6 \times 10^{-3}~G_0~(\approx 124~\rm nS)$  and  $\approx 7.9 \times 10^{-6}~G_0~(\approx 0.61~\rm nS)$ , achieving a high on/off ratio exceeding two orders of magnitude (Figure 4c). This highlights its potential as a mechanically controlled molecular switch. Moreover, the molecular conductance switching exhibits consistent statistical on/off ratios across different oscillation frequencies (Figure 4c, inset), highlighting the robustness of the B $\leftarrow$ N coordinated molecular switch.

In addition to direct mechanical regulation, electric fields have been shown to significantly regulate  $\pi$ -stacking in supramolecular dimers.[10] To quantitatively assess the noncovalent interactions between the orthogonal  $\pi$ -electron clouds of the two stereoconformations of DPA, voltage-dependent single-molecule electrical measurements (Figure S38, Supporting Information) and energy component analysis are conducted. Figure 4d presents the 1D conductance histograms of DPA under source-drain voltages ranging from 0.05 to 0.25 V with a 0.05 V step size. Consistent with previous I-V analyses, the molecular conductance shows minimal shifts in the low-bias region. At 0.25 V, S1-DPA begins to exhibit conductance enhancement. However, the conductance peak area of S1-DPA significantly increases with the electric field, rising from 0.26 to 0.51 relative to the total peak areas (Figure \$39, Supporting Information). This variation indicates that the stability of the two stacking modes differs, with distinct interactions between stacking regions and the boraacene center.

To further understand the origin of these distinctive characteristics between different stacking structures, the interaction energy decomposition into different physical components is conducted using the symmetry-adapted perturbation theory (Figure 4e; Figures S40 and S41, Supporting Information).[41,42] As the electric field increases, the total weak interaction forces of S1-DPA are distinctly higher than those of S2-DPA, which tend to stabilize S1-DPA with the increasing electric field. [36] Notably, S1-DPA exhibits a significant increase in exchange energy between the thiomethylphenyl dimer and boraacene due to the fieldenhanced spatial overlap between the  $\pi$ - $\pi$  stacked dimers and boraacene, demonstrating electronic coupling between orthogonal  $\pi$  electron clouds. [41] In contrast, S2-DPA exhibits a stronger increase in induction energy between the t-BuPy dimer and boraacene, which can be attributed to the field-induced increase in dipole moment within the B←N dative structures.<sup>[43]</sup> These analyses reveal the distinct roles of exchange- and inductiondominated interactions in stabilizing the stereostructures of the all-carbon-based stacking and B←N-coordinated stacking systems, respectively, under applied electric fields.

In addition to the modulation of external electric fields, substituent effects are proposed to tune the electronic properties of B←N structures. [44] STM-BJ measurements on diverse 4-substituted pyridine-adducted systems with different electron-withdrawing and electron-donating structures (Figure S42, Supporting Information) are performed. Figure 4f depicts the 1D conductance histograms of B←N structures with different substituents, which exhibit two conductance states that are designated similarly to the wing-opening and wing-closing conformations of the previously discussed butterfly-shaped CMe<sub>3</sub>-DPA (Figure 2), respectively. Both S1 and S2 states of DPA with electron-donating substituents, such as the trimethoxy methyl

group (-C(OMe)<sub>3</sub>), exhibit conductance behaviors comparable to CMe<sub>3</sub>-DPA, with an enhanced conductance for S1. In contrast, electron-withdrawing substituents, such as trichloromethyl (—CCl<sub>3</sub>) and trifluoromethyl (—CF<sub>3</sub>) groups, increase the stability of higher conductance states, while reducing the overall conductance. Further theoretical transmission spectra reveal that electron-donating substituents increase molecular conductance by shifting the *p*-HOMO closer to the Fermi level, consistent with the experimental results (Figures S43–S46 and Table S4, Supporting Information). The trend is mainly attributed to electronic effects rather than steric hindrance (Table S5, Supporting Information). In addition, the relative energy difference (Figure 4f, inset) between S1 and S2 states reveals that electron-withdrawing units reduce the stability of S2, likely due to increased repulsion between pyridine dimers.

#### 2.5. Dynamic Regulation of B←N Coordinated DPP Junctions

In comparison with boraacene, borapentacene exhibits stronger conjugation, offering direct control over the electronic properties and charge distribution of the B←N structure. [45] Introducing borapentacene as the acene core in the B←N structures enables the investigation of how the orthogonal  $\pi$  electron clouds affect electronic properties and dynamic regulation.<sup>[27]</sup> Similar to DPA, the nucleophilic attack of t-BuPy on the borapentacene core forms a B←N dative bond, yielding the doubly pyridine-substituted borapentacene (DPP) structure (Figure 5a). While electrostatic potential surfaces of DPP reveal a higher electron deficiency in the borapentacene region in comparison with DPA (Figure S47, Supporting Information), the 2D conductance histograms obtained from STM-BJ measurements (Figure 5b) and the typical single trace (fitting in Figure 5b; Figure S48, Supporting Information) show two conductance peaks similar to those observed for DPA. The corresponding 1D conductance histograms (Figure 5c) display two Gaussian-fitted peaks at  $\approx 5.0 \times 10^{-5}$   $G_0$  ( $\approx 3.9$  nS) and  $\approx 2.0 \times 10^{-6}$   $G_0$  ( $\approx 0.16$  nS), respectively. The *I–V* characteristics and Fowler-Nordheim plots of DPP are further analyzed in Figures \$49 and \$50 (Supporting Information).

Analogous to the mechanically controlled switching between wing-opening and wing-closing conformations observed in DPA, DPP also exhibits a higher conductance state associated with thiomethylphenyl  $\pi$ – $\pi$  stacking (S1-DPP) and a lower conductance state involving t-BuPy  $\pi$ - $\pi$  stacking (S2-DPP), as demonstrated by the theoretical potential energy surface calculations (Figure \$51, Supporting Information). These stacking behaviors are corroborated by MPSH and transmission eigenstate analyses (Figures S52 and S53, Supporting Information). The molecular conductance of both S1-DPP and S2-DPP is reduced compared to their DPA counterparts. Notably, the HOMO distribution of DPP is significantly more localized on the borapentacene region than that of the boraacene region in DPA (Figure S54, Supporting Information), which suggests a higher involvement of orthogonal  $\pi$  electrons in borapentacene during charge transport, therefore accounting for the conductance decline. Flicker noise analysis (Figure 5b, inset; Figure \$55, Supporting Information) supports this observation, revealing a more through-bond transport for S1-DPP (N = 1.8) compared to S1-DPA (N = 1.9).[34]

15214095, 0, Downloaded from https://advanced.onlinelibrary.wiley.com/doi/10.1002/adma.202504455 by Peking University Health, Wiley Online Library on [02/11/2025]. See the Terms and Conditions (https://onlinelibrary.wiley.com/terms/

and-conditions) on Wiley Online Library for rules of use; OA articles are governed by the applicable Creative Commons

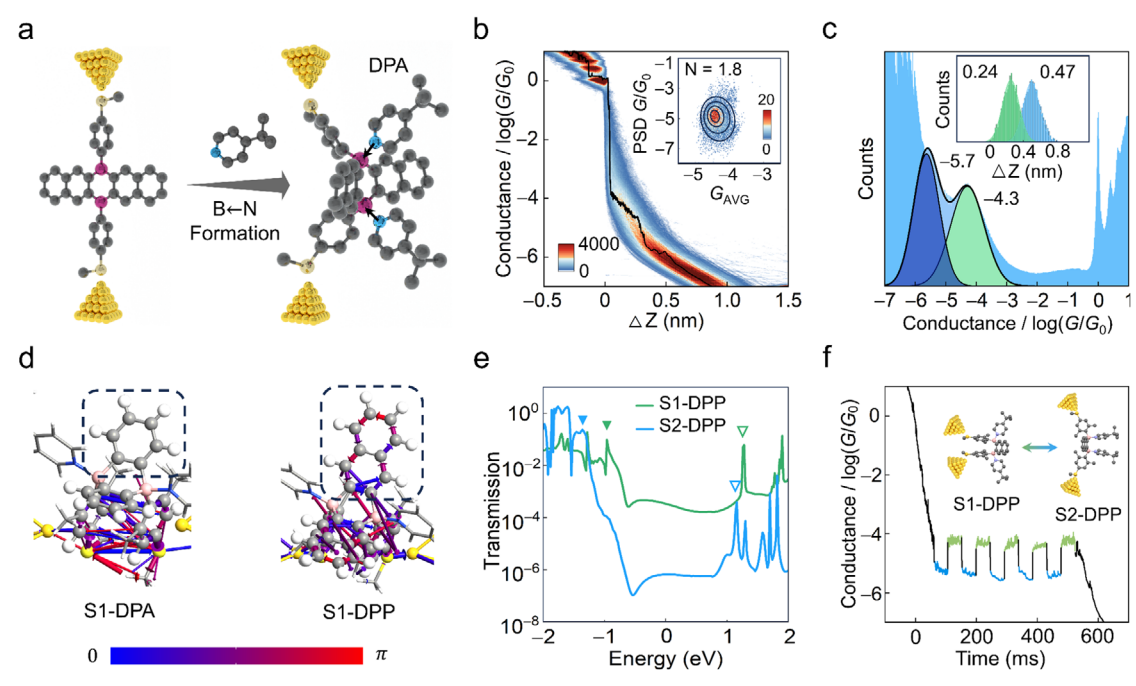


**Figure 5.** Single-molecule electrical measurements and theoretical analyses of DPP. a) Schematic diagram of borapentacene coordinated with pyridine to form DPP structures. b) 2D conductance-displacement histograms of DPP obtained from STM-BJ measurements, with a color bar indicating the number of counts. A typical single trace of DPP, displaying two distinct conductance states, is highlighted. The inset shows 2D histograms of normalized noise power versus average conductance for the higher conductance state (S1) of DPP. c) 1D conductance histograms of DPP junctions, with an inset presenting the normalized plateau-length distributions measured within respective ranges. d) Theoretical transmission pathways of p-HOMOs in S1-DPA and S1-DPP and junctions, with the color bar indicating forward (blue) and backward (red) transmission. Dashed outlines highlight the boracacene and borapentacene regions, which contribute to constructive and destructive quantum interference, respectively. e) Transmission spectra of S1-DPP and S2-DPP, with triangles marking the transmission peaks corresponding to *p*-HOMOs and *p*-LUMOs. f) Typical conductance-time trace of DPP under square-wave oscillations, with S1 and S2 states indicated by different colors. The inset depicts a schematic of DPP undergoing stretching and compression, leading to bistable state switching.

In addition to the orthogonal  $\pi$ -electron localization, the calculated transmission spectra reveal that the reduced conductance in both states of DPP is also due to destructive quantum interference (DOI), which lowers the transmission probability near the Fermi level (Figure 5e; Figure S56, Supporting Information). DQI occurs when electron tunneling through discrete molecular orbitals results in out-of-phase wavefunction superposition, leading to diminished conductance. [25,46] The origins of DOI in DPP junctions are further understood by transmission pathway analysis of p-HOMOs, as shown in Figure 5d.[47,48] In the p-HOMO transmission pathways of S1-DPA, the boraacene region is less involved in charge transport. In contrast, the borapentacene region of S1-DPP exhibits strong backward transmission, which contributes to DQI and hinders charge transport efficiency.<sup>[47,49]</sup> The transmission pathways of both the p-HOMO and *p*-LUMO in S2-DPP corroborate this pattern (Figures \$57 and \$58, Supporting Information). These findings highlight the versatility of B←N-coordinated molecules in enabling quantum effects through modulation of the central boron-containing

DPP can also be used to fabricate mechanically controlled reversible molecular switches. Under a 20 Hz square-wave oscillation, the typical single trace of DPP exhibits conductance switching between  $\approx 5.0 \times 10^{-5}~G_0~(\approx 3.9~\text{nS})$  and  $\approx 3.2 \times 10^{-6}~G_0~(\approx 0.25~\text{nS})$  (Figure 5f). The corresponding 2D G–t histograms

for the square-wave oscillation are exhibited in Figure S59 (Supporting Information). The observed switching behavior highlights the stability and versatility of dynamically regulated  $B \leftarrow N$  stereostructures, thereby supporting their potential for adaptive molecular device applications.

### 3. Conclusion

We propose a general strategy for multiunit molecular design via B←N coordination and achieve dynamic regulation of the butterfly-shaped stereostructures. By combining STM-BJ experiments and first-principles calculations, through-space and through-bond transport mechanisms under different conformations are demonstrated with single-molecule precision. Mechanical control facilitates robust single-molecule switching with on/off ratios exceeding 100. Moreover, external electric fields and substituent effects further tune the electronic characteristics and transport efficiency of the B←N stereostructures. Expanding the acene core and interacting  $\pi$ -electron clouds introduces quantum interference effects, which alter transport pathways and enhance molecular functional versatility. These findings underscore the significance of dynamic regulation of multiunit B←N molecules in achieving tailored molecular properties, which exhibit robust and multimodal responses to external stimuli, paving the way

15214095, 0, Downloaded from https://advanced.onlinelibrary.wiley.com/doi/10.1002/adma.202504455 by Peking University Health, Wiley Online Library on [02/11/2025]. See the Terms and Conditions (https://onlinelibrary.wiley.com/terms-

-and-conditions) on Wiley Online Library for rules of use; OA articles are governed by the applicable Creative Commons

for advanced applications in molecular electronics and smart materials.

## 4. Experimental Section

Materials and Characterization: The gold substrates utilized in the STM-BJ experiments were prepared using a magnetron sputtering system. Silicon wafers with SiO<sub>2</sub> surfaces were first coated with a 10 nm chromium layer to enhance contact quality, followed by the deposition of a 200 nm gold layer. The STM gold tips were fabricated from 99.99% pure gold wires (0.25 mm in diameter, purchased from ZhongNuo Advanced Materials, Beijing) through electrochemical etching at an applied voltage of 1.2 V. All solvents, obtained from Shanghai Aladdin Biochemical Technology Co., Ltd., were used as received without further purification.

STM-BJ Measurement: The STM-BJ technique measures the electrical conductance of single molecules by repeatedly forming and breaking Au-molecule-Au junctions with a stepper motor and piezoelectric stack. The process began with bringing a sharp STM tip and the gold electrode into proximity with a molecule at room temperature and atmospheric pressure. As the electrode was retracted, the gold junction narrowed, and the molecule stretched, forming an anchor-to-anchor molecular junction before breakage. Conductance was recorded as a function of tip displacement just prior to junction rupture. Thousands of individual traces containing molecular conductance data were collected to construct 2D conductance-displacement histograms, which were further analyzed to extract 1D conductance histograms and plateau lengths. The data collected during the tip's approach to the substrate plays a critical role in subsequent analyses. The data analyses were conducted using the open-source software available at https://github.com/Pilab-XMU/ XMe\_DataAnalysis.<sup>[50]</sup> All experiments were performed at room temperature using the Xtech STM-BJ instrument developed by Professor Wenjing Hong's research group at Xiamen University.

I-t and I-V Measurements: As the STM tip approached the molecular junction, its motion was halted once a stable conductance plateau was established within a predefined range, ensuring junction stability. With the bias voltage held constant, *I-t* data were collected in this "hovering" state to monitor conductance as a function of time. The I-t data were then converted to G-t data for further analyses. To analyze flicker noise, power spectral densities were calculated by squaring the discrete Fourier transform of conductance traces recorded during the break-junction process. The spectra were integrated over 100-1000 Hz and normalized by the square of the average conductance. This allowed the construction of a 2D histogram plotting normalized noise power versus average conductance, enabling comparison of noise characteristics across different transport regimes.

Once the molecular junction stabilized, a square wave voltage signal was applied to the piezoelectric actuator between the STM tip and substrate. This oscillation alternated between high and low voltage states, inducing periodic stretching and retraction of the molecular junction. During these oscillations, the junction's conductance was continuously recorded over time, facilitating the generation of 2D conductance-time histograms.

In the stabilized hovering state, I-V measurements were performed by applying a bias voltage between the tip and substrate, sweeping from -1.0 to 1.0 V in increments of 0.5 mV. This voltage sweep enabled a detailed current-voltage analysis of the molecular junction's electronic properties, represented as 2D current-voltage histograms. The I-V data were further analyzed to derive Fowler-Nordheim (FN) tunneling plots, providing deeper insights into the electronic transport behavior of the molecular junction.

Theoretical Calculations: DFT calculations were performed using the Gaussian 16 package to optimize the geometric structures of all target molecules. The B3LYP hybrid functional with a 6-31G(d) basis set was employed, incorporating dispersion corrections at the GD3 (BJ) level.<sup>[51,52]</sup> Relaxed coordinate scan and binding energies were calculated with the same precision. Orbital visualization and analysis were conducted using GaussView, while graphics were generated using Multiwfn and VMD software. [53] SAPT calculations were performed using PSI-4 software, as detailed in the Supporting Information.<sup>[42]</sup>

Charge transport properties of the molecular junctions were investigated within the DFT-based non-equilibrium Green's function (NEGF-DFT) formalism, implemented in QuantumATK.[54] The interfacial conformation between molecules and gold electrodes was optimized using the L-BFGS algorithm. NEGF-DFT calculations employed FHI pseudopotentials and a double-zeta polarized atomic orbital basis set, with exchangecorrelation effects treated at the GGA-PBE level. Self-consistency was achieved when Hamiltonian and density matrix elements converged below  $10^{-5}$  atomic units. Transmission spectra were computed with a 15 imes15 k-point sampling. Molecular energy spectra, molecular projected selfconsistent Hamiltonian (MPSH) spectra, transmission eigenstates, and transport pathways near the gold Fermi level were analyzed to elucidate dominant charge transport channels.

## **Supporting Information**

Supporting Information is available from the Wiley Online Library or from the author.

## **Acknowledgements**

The authors acknowledged financial support from the National Key R&D Program of China (2024YFA1208100, 2021YFA1200102, 2021YFA1200101, 2023YFF1205803, and 2022YFE0128700), the National Natural Science Foundation of China (22173050, 22375106, and 22071120), the Haihe Laboratory of Sustainable Chemical Transformations, and Beijing National Laboratory for Molecular Sciences (BNLMS-CXXM-202407).

#### **Conflict of Interest**

The authors declare no conflict of interest.

### **Author Contributions**

B.W., Y.H., and C.C. contributed equally to this work. X.G., C.J., J.W., and X.W. conceived the idea for the paper. B.W. and Y.H. carried out the experimental measurements. C.C. carried out the molecular synthesis. B.W. and Y.H. built and analyzed the theoretical model and performed the quantum transport calculation. B.W. drew the diagrams. X.G., C.J., J.W., X.W., B.W., Y.H., and C.C. analyzed the data and wrote the paper. All the authors discussed the results and commented on the manuscript.

## **Data Availability Statement**

The data that support the findings of this study are available from the corresponding author upon reasonable request.

## Keywords

B←N coordination, charge transport, dynamic regulation, quantum interference, single-molecule junction

> Received: March 5, 2025 Revised: August 29, 2025 Published online:

<sup>[1]</sup> L. Feng, R. D. Astumian, J. F. Stoddart, Nat. Rev. Chem. 2022, 6, 705.

<sup>[2]</sup> B. S. Gomes, B. Simões, P. M. Mendes, Nat. Rev. Chem. 2018, 2, 0120.

5214095, 0, Downloaded

from https

- [3] S. Krause, B. L. Feringa, Nat. Rev. Chem. 2020, 4, 550.
- [4] J. Chen, Q. Peng, X. Peng, H. Zhang, H. Zeng, Chem. Rev. 2022, 122, 14594.
- [5] X. Li, Q. Wu, J. Bai, S. Hou, W. Jiang, C. Tang, H. Song, X. Huang, J. Zheng, Y. Yang, J. Liu, Y. Hu, J. Shi, Z. Liu, C. J. Lambert, D. Zhang, W. Hong, Angew. Chem., Int. Ed. 2020, 59, 3280.
- [6] D. Sluysmans, F. Devaux, C. J. Bruns, J. F. Stoddart, A.-S. Duwez, Proc. Natl. Acad. Sci. U.S.A. 2017, 115, 9362.
- [7] S. Borsley, J. M. Gallagher, D. A. Leigh, B. M. W. Roberts, *Nat. Rev. Chem.* 2023, 8, 8.
- [8] S. Borsley, D. A. Leigh, B. M. W. Roberts, Angew. Chem., Int. Ed. 2024, 63, 202400495.
- [9] P. Li, S. Hou, B. Alharbi, Q. Wu, Y. Chen, L. Zhou, T. Gao, R. Li, L. Yang, X. Chang, G. Dong, X. Liu, S. Decurtins, S.-X. Liu, W. Hong, C. J. Lambert, C. Jia, X. Guo, J. Am. Chem. Soc. 2022, 144, 15689
- [10] Y. Tang, Y. Zhou, D. Zhou, Y. Chen, Z. Xiao, J. Shi, J. Liu, W. Hong, J. Am. Chem. Soc. 2020, 142, 19101.
- [11] A. Feng, Y. Zhou, M. A. Y. Al-Shebami, L. Chen, Z. Pan, W. Xu, S. Zhao, B. Zeng, Z. Xiao, Y. Yang, W. Hong, Nat. Chem. 2022, 14, 1158.
- [12] X. Li, W. Ge, S. Guo, J. Bai, W. Hong, Angew. Chem., Int. Ed. 2023, 62, 202216819.
- [13] X. Li, Y. Zheng, Y. Zhou, Z. Zhu, J. Wu, W. Ge, Y. Zhang, Y. Ye, L. Chen, J. Shi, J. Liu, J. Bai, Z. Liu, W. Hong, J. Am. Chem. Soc. 2023, 145, 21679.
- [14] C. Hsu, W. M. Schosser, P. Zwick, D. Dulić, M. Mayor, F. Pauly, H. S. J. van der Zant, Chem. Sci. 2022, 13, 8017.
- [15] J. Li, P. Shen, S. Zhen, C. Tang, Y. Ye, D. Zhou, W. Hong, Z. Zhao, B. Z. Tang, Nat. Commun. 2021, 12, 167.
- [16] M. Carini, M. P. Ruiz, I. Usabiaga, J. A. Fernández, E. J. Cocinero, M. Melle-Franco, I. Diez-Perez, A. Mateo-Alonso, *Nat. Commun.* 2017, 8 15195
- [17] L. Chen, Y. H. Wang, B. He, H. Nie, R. Hu, F. Huang, A. Qin, X. S. Zhou, Z. Zhao, B. Z. Tang, Angew. Chem., Int. Ed. 2015, 54, 4231.
- [18] C. Wu, D. Bates, S. Sangtarash, N. Ferri, A. Thomas, S. J. Higgins, C. M. Robertson, R. J. Nichols, H. Sadeghi, A. Vezzoli, *Nano Lett.* 2020, 20, 7980.
- [19] J. Huang, X. Wang, Y. Xiang, L. Guo, G. Chen, Adv. Energy Sustain. Res. 2021, 2, 2100016.
- [20] K. Ariga, T. Mori, J. P. Hill, Adv. Mater. 2011, 24, 158.
- [21] S. Y. Chen, Z. H. Zhao, C. H. Li, Q. Li, Responsive Mater. 2023, 1, 20230011.
- [22] G. Campillo-Alvarado, K. P. D'Mello, D. C. Swenson, S. V. Santhana Mariappan, H. Höpfl, H. Morales-Rojas, L. R. MacGillivray, Angew. Chem., Int. Ed. 2019, 58, 5413.
- [23] C.-H. Liu, L. Chen, H. Zhang, Y. Li, H. Lin, L. Li, J. Wu, C. Liu, Z.-M. Ye, S. Xiang, B. Chen, Z. Zhang, Chem 2023, 9, 3532.
- [24] D. Xiang, X. Wang, C. Jia, T. Lee, X. Guo, Chem. Rev. 2016, 116, 4318.
- [25] T. A. Su, M. Neupane, M. L. Steigerwald, L. Venkataraman, C. Nuckolls, Nat. Rev. Mater. 2016, 1, 16002.
- [26] N. Xin, J. Guan, C. Zhou, X. Chen, C. Gu, Y. Li, M. A. Ratner, A. Nitzan, J. F. Stoddart, X. Guo, *Nat. Rev. Phys.* **2019**, *1*, 211.
- [27] C. Chen, M. W. Wang, X. Y. Zhao, S. Yang, X. Y. Chen, X. Y. Wang, Angew. Chem., Int. Ed. 2022, 61, 202200779.

- [28] L. Palomino-Ruiz, S. Rodríguez-González, J. G. Fallaque, I. R. Márquez, N. Agraït, C. Díaz, E. Leary, J. M. Cuerva, A. G. Campaña, F. Martín, A. Millán, M. T. González, Angew. Chem., Int. Ed. 2021, 60, 6609.
- [29] L. Bai, Y. Ma, X. Jiang, J. Am. Chem. Soc. 2021, 143, 20609.
- [30] D. Jariwala, T. J. Marks, M. C. Hersam, Nat. Mater. 2017, 16, 170.
- [31] K. Wang, B. Xu, Top. Curr. Chem. 2017, 375, 17.
- [32] P. Li, L. Zhou, C. Zhao, H. Ju, Q. Gao, W. Si, L. Cheng, J. Hao, M. Li, Y. Chen, C. Jia, X. Guo, Rep. Prog. Phys. 2022, 85, 086401.
- [33] S. Li, H. Yu, J. Li, N. Angello, E. R. Jira, B. Li, M. D. Burke, J. S. Moore, C. M. Schroeder, *Nano Lett.* **2021**, *21*, 8340.
- [34] O. Adak, E. Rosenthal, J. Meisner, E. F. Andrade, A. N. Pasupathy, C. Nuckolls, M. S. Hybertsen, L. Venkataraman, *Nano Lett.* 2015, 15, 4143.
- [35] X. Wei, X. Chang, J. Hao, F. Liu, P. Duan, C. Jia, X. Guo, J. Am. Chem. Soc. 2024, 146, 26095.
- [36] H. Ju, B. Wang, M. Li, J. Hao, W. Si, S. Song, K. Mei, A. C. Sue, J. Wang, C. Jia, X. Guo, J. Am. Chem. Soc. 2024, 146, 25290.
- [37] E. J. Dell, B. Capozzi, K. H. DuBay, T. C. Berkelbach, J. R. Moreno, D. R. Reichman, L. Venkataraman, L. M. Campos, J. Am. Chem. Soc. 2013, 135, 11724.
- [38] C. Yang, Y. Guo, H. Zhang, X. Guo, Chem. Rev. 2025, 125, 223.
- [39] J. M. Beebe, B. Kim, J. W. Gadzuk, C. D. Frisbie, J. G. Kushmerick, Phys. Rev. Lett. 2006, 97, 026801.
- [40] D. Stefani, K. J. Weiland, M. Skripnik, C. Hsu, M. L. Perrin, M. Mayor, F. Pauly, H. S. J. van der Zant, *Nano Lett.* 2018, 18, 5981.
- [41] M. J. Phipps, T. Fox, C. S. Tautermann, C. K. Skylaris, Chem. Soc. Rev. 2015, 44, 3177.
- [42] D. G. A. Smith, L. A. Burns, A. C. Simmonett, R. M. Parrish, M. C. Schieber, R. Galvelis, P. Kraus, H. Kruse, R. Di Remigio, A. Alenaizan, A. M. James, S. Lehtola, J. P. Misiewicz, M. Scheurer, R. A. Shaw, J. B. Schriber, Y. Xie, Z. L. Glick, D. A. Sirianni, J. S. O'Brien, J. M. Waldrop, A. Kumar, E. G. Hohenstein, B. P. Pritchard, B. R. Brooks, H. F. Schaefer III, A. Y. Sokolov, K. Patkowski, A. E. DePrince III, U. Bozkaya, et al., J. Chem. Phys. 2020, 152, 184108.
- [43] T. M. Parker, L. A. Burns, R. M. Parrish, A. G. Ryno, C. D. Sherrill, J. Chem. Phys. 2014, 140, 094106.
- [44] F. Chen, Q.-M. Liang, L.-X. Lin, Q.-C. Zhang, Y. Yang, J. Mater. Chem. C 2023, 11, 14515.
- [45] E. Grotthuss, A. John, T. Kaese, M. Wagner, Asian J. Org. Chem. 2017, 7. 37.
- [46] J. Liu, X. Huang, F. Wang, W. Hong, Acc. Chem. Res. 2018, 52, 151.
- [47] G. C. Solomon, C. Herrmann, T. Hansen, V. Mujica, M. A. Ratner, Nat. Chem. 2010, 2, 223.
- [48] P. Gehring, J. M. Thijssen, H. S. J. van der Zant, Nat. Rev. Phys. 2019, 1, 381.
- [49] S. van der Poel, J. Hurtado-Gallego, M. Blaschke, R. Lopez-Nebreda, A. Gallego, M. Mayor, F. Pauly, H. S. J. van der Zant, N. Agrait, Nat. Commun. 2024, 15, 10097.
- [50] Z. Pan, G. Dong, C. Shang, R. Li, T. Gao, L. Lin, H. Duan, X. Li, J. Bai, Y. Lai, W. Wu, J. Shi, J. Liu, W. Hong, Chin. J. Chem. 2024, 42, 317.
- [51] A. D. Becke, J. Chem. Phys. 1993, 98, 5648.
- [52] J. Taylor, H. Guo, J. Wang, Phys. Rev. B 2001, 63, 245407.
- [53] T. Lu, F. Chen, J. Comput. Chem. 2011, 33, 580.
- [54] M. Brandbyge, J.-L. Mozos, P. Ordejón, J. Taylor, K. Stokbro, *Phys. Rev. B* 2002, 65, 165401.